

We are IntechOpen, the world's leading publisher of Open Access books Built by scientists, for scientists

5,800

Open access books available

142,000

International authors and editors

180M

Downloads

Our authors are among the

154

Countries delivered to

TOP 1%

most cited scientists

12.2%

Contributors from top 500 universities



WEB OF SCIENCE™

Selection of our books indexed in the Book Citation Index
in Web of Science™ Core Collection (BKCI)

Interested in publishing with us?
Contact book.department@intechopen.com

Numbers displayed above are based on latest data collected.
For more information visit www.intechopen.com



Integrated Optics and Photonics for Optical Interferometric Sensing

Marco Chiarini, Alberto Parini and Gian Giuseppe Bentini

Abstract

Integrated optics (IO) microsystems, based on guided wave and photonics structures, can find interesting developments for optical interferometric analysis in sensing applications. In fact, IO interferometric microsystems can act as transducers of the information carried on by an optical signal and originated along the signal optical path. In addition, the application of Integrated Optics and Photonics techniques, allow producing very small size and reduced power consumption instrumentation. These features explain the reason why the IO microsystems for interferometric analytics know an increasing interest in many areas such as Astrophysics, Environment, Biosciences, Space and Earth Exploration, Safety and Security. This chapter starts by synthetically describing the basics of the main analytical techniques covered by IO micro-devices. A discussion of the integrated micro-device fabrication procedures, with an analysis of the implied performance limitations, follows. Finally, a description of new generation optical interferometric microsystems, applied to different scientific and technical areas, completes the chapter.

Keywords: optical interferometry, Fourier transform interferometry, integrated optics, photonics, integrated optical sensors, Mach–Zehnder micro-interferometers, MEOS sensing devices

1. Introduction

There is a growing interest in finding detection technologies enabling real-time and on-line monitoring of many elements having remarkable, (in some cases dramatic), impacts on our everyday lives. Consequently, a huge effort has been devoted to designing and building instruments with capabilities that would not even be thought of a few years ago. Nowadays are required instruments to analyse many fields of high interest ranging from environmental pollutants or pathogens in air and water, up to the Security and Safety in the urban ambient or in the logistic chain of food production and transport, as well as many other applications.

In most cases, the realisation of this kind of device involves analytical techniques that should avoid chemical reactants, difficult to be used outside specialised laboratories. Moreover, the device has to be routinely applied by almost untrained people that should also be able to read and understand the measurement result. At the same time, the analytical equipment must be self-contained and available at a very low cost.

Nowadays, the only available solution suitable to satisfy the whole of these requirements is to develop highly miniature integrated equipment to allow mass production using technologies likewise the planar technologies driven by the development of microelectronics. At the present state of the art, most of these requirements can be satisfied when it is possible to develop sensing techniques belonging to the family of the optical integrated microdevices.

Optical detection can concern different properties of light such as Intensity, (in the case of photometric analyses), Wavelength, (in the case of spectroscopic analyses), Refractive Index, (in the case of Index change due to the presence of the analyte molecules at the Sensor Surface), etc.

A large variety of optical and photonic microdevices, based on interferometric, energy dispersive elements, photonic micro and nanofluidic devices, has been designed, studied and reported in the literature [1–6].

The development at industrial quality level of active optical materials, (particularly Lithium Niobate, LiNbO_3), joined to the use of planar technology, has allowed the fabrication of monolithic integrated optical microdevices having sensing capabilities comparable to the correspondent standard laboratory equipment.

As highlighted in the next paragraphs, IO and Photonics microfabrication techniques, offer the possibility to generate in monolithic and miniaturised systems, nearly all the equivalents of classical optical components (mirrors, splitters, combiners, phase shifters, etc.). Furthermore, such IO components can be integrated into and interfaced with guided wave circuits, such as integrated optical waveguides and optical fibres. These characteristics often strongly simplify all issues related to optical alignment and maintenance, the flow of the luminous signal, carrying the information, being firmly confined within fixed and well defined optical channels. In the following an overview of the characteristics and potentialities of IO devices is presented, in particular for a wide range of interferometric sensing applications.

2. Basic principles of IO for interferometric sensing

The basic element of any Integrated Optic device is the optical waveguide that can be generated by tailoring the refractive index (n) in the near-surface region of the base material. It must be remembered that the light transmission is confined in the regions where the refractive index is higher than in the surroundings.

Several techniques have been developed to obtain local variation of the refractive index creating the possibility to obtain an integrated optical waveguide. In this chapter, we will only mention some of the most common techniques used for LiNbO_3 substrate, which is one of the most used materials in optical device fabrication. One possibility is to use local doping processes obtained by photolithographic definition of the desired waveguide geometry associated with the dopant thermal diffusion (typically, Ti diffusion or Proton exchange processes), to increase the refractive index in the doped region. Alternatively, it is possible to create a waveguide by lowering the refractive index of the base material in the regions outside the waveguide introducing lattice damage through ion bombardment. A third possibility is to pattern the surface with the desired geometry, and etching the surrounding region to obtain a ridge waveguide protruding from the surface. **Figure 1** reports a sketch of the two geometries.

In general, the geometries of the integrated microsystems are designed to reproduce the same physical effects obtained by optical instrumental architectures created in laboratory, assembling several optical elements like mirrors, beam splitters, etc.

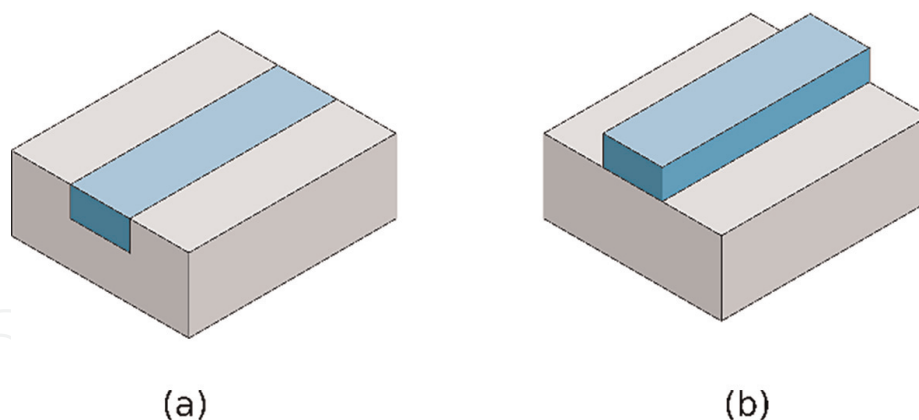


Figure 1.
Two basic geometries of integrated optics waveguides: (a) buried waveguide, (b) ridge waveguide.

Probably, the most frequently used integrated micro-spectrometric devices are based on the Mach-Zehnder Interferometric, (MZI), geometry [1–4] or on Young Interferometer, (YI) or, more recently, on the Staircase Micro Diffractive Gratings, (MDG) first developed by Michelson [5].

All these devices take advantage of the Electro-Optic properties of the LiNbO_3 substrate. In fact, the optoelectronic properties of the substrate allow to locally controlling the refractive index of a waveguide by applying a suitable electric field, so creating a Pockels cell that induces a phase modulation in the light transmitted in the specific waveguide (See **Figure 2**).

In particular, it can be useful to recall that, in the case of spectroscopic analysis techniques, the wavelength-dispersive systems, such as prisms or gratings, spatially spread the light wavelengths at different angles allowing the direct measurements of the relative intensities, (wavelength spectrum), by using suitable photodetectors at the corresponding angles.

On the contrary, in the Fourier Transform Spectroscopy the intensity of the total light beam that contains the whole ensemble of wavelength, at the same time, is measured. In this case, the measurement with a traditional Mach-Zehnder instrument is performed by splitting the light beam into two branches that are then recombined giving rise to an interference pattern. The light intensity of the recombined beams is

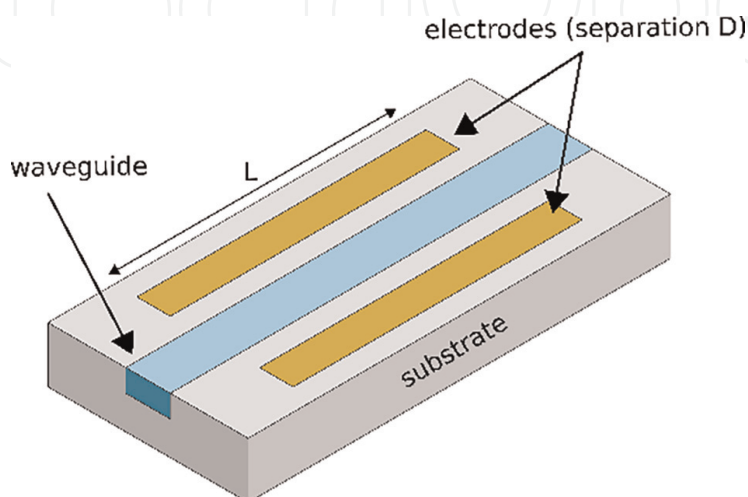


Figure 2.
Integrated version of a Pockels cell to be used as a phase modulator.

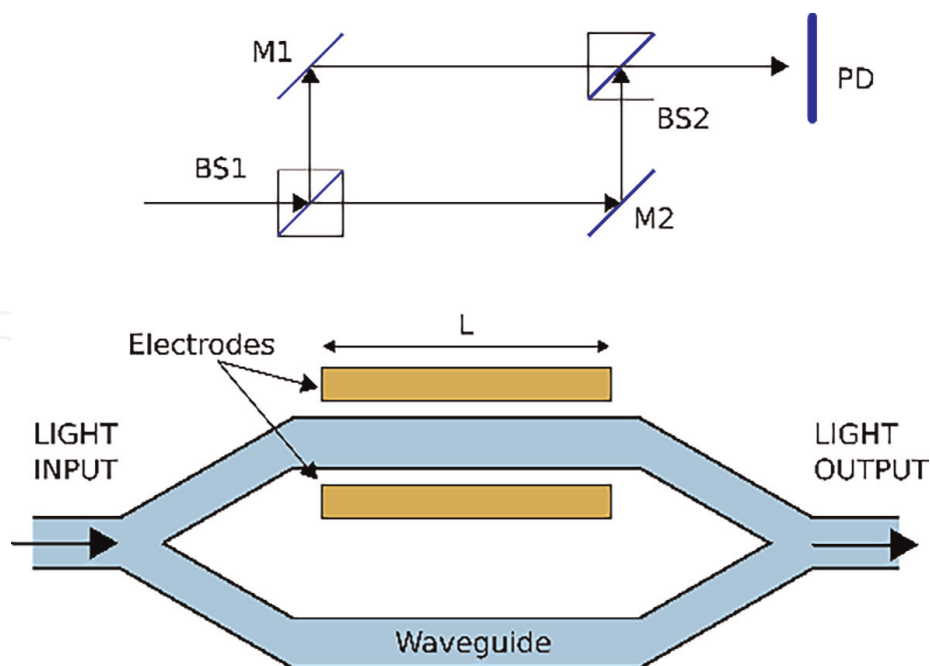


Figure 3. Upper: Traditional Mach-Zehnder interferometer geometry. The light beam first crosses the BS1 beam splitter then, through the M1 and M2 mirrors, the two light beams are recombined in BS2 and then arrive in the photodetector PD. lower: Equivalent integrated optic device: The voltage applied to the electrodes controls the phase shift in the light beams propagating in the two arms.

measured as a function of the phase shift, generated by the respective different optical path-lengths $l = nL$, where n is the refractive index and L is the geometrical path length.

Figure 3(a), reports a typical example of Mach-Zehnder equipment, whereas Figure 3(b) is shown the equivalent device fabricated with planar technology. Following the optical interference laws, the intensity measured by the photodetector (PD) depends on the phase shift between the two optical paths. Inducing a variation in the optical paths, l , of one of the two arms the phase shift changes and, in turn, the correspondent variation of the light intensity is measured by the PD.

3. Photonic integrated interferometers for chemical and biological sensing

Actually, due to the relatively simple design, the Mach-Zehnder Interferometer, (MZI), is the most adequate configuration for the monolithic fabrication of integrated optics microsensors. In fact, this structure is particularly suitable for sensing problems as it can combine high resolution and high sensitivity performances together with an excellent insensitiveness on mechanical vibration or other environmental effects. Many applications of optical sensors based on MZ interferometer have been reported in literature, both in the case of already cited Fourier Transform, (FT), and spectroscopy. In the case of Bio-chemical analyses, the phase shift between the electromagnetic waves propagating in the two arms of the MZI is generated by the adhesion of the analyte molecules on the surface of one (sensing) arm that has been left uncovered by the cladding protecting the whole device from the environment [4–6]. The working principle, in this case, is based on the optical path variation, $\Delta p = \Delta nL$, generated by the change of the refractive index in the uncovered sensing arm, having a length L . A relatively limiting factor of this instrumental architecture is originated from the

need for a relatively large value of the sensing interferometric arm L , to have a good sensitivity of the device. Moreover, to obtain the best performances of an MZI in terms of sensitivity, requires working with monochromatic light, for this reason, it has been suggested [6] to design a hybrid detection architecture, specifically oriented to biochemical applications, allowing both high sensitivity and a high selectivity in the case of multi-analyte detection. This performance can be obtained by integrating an MZ interferometer with a spectrum analyser and using a multi-wavelength 'white' light source to distinguish the spectral 'signature' of the different species. **Figure 4** is redrawn the device originally suggested in Ref. [7].

As previously anticipated, when the monolithic interferometer is fabricated on Electro-optic material, typically LiNbO_3 , the phase shift can be generated by exploiting the Pockels effect to modify the refractive index in one of the two arms, through the application of an electric field using two electrodes placed in a suitable position close to the optical waveguide (see **Figure 3(b)**).

If a continuous variation of the phase shift is generated, it is realised a so-called scanning interferometer and the whole set of intensity data measured as a function of the phase shifts gives rise to the so-called Interferogram. The Fourier Transform of the Interferogram gives rise to the frequency spectrum of the light containing the spectral information on the element to be detected [3, 4]. In the traditional instrument of **Figure 3(a)** the scanning effect is usually produced by uniformly moving one of the two mirrors giving rise to a corresponding optical path variation in one arm of the interferometer generating the desired phase shift variation. On the contrary, in an integrated microdevice, the scanning effect can be simply obtained by applying a voltage ramp to the electrodes (see **Figure 3(b)**), without the need for moving parts.

The detailed description of the Fourier Transform Spectroscopy principle and the detailed mathematical considerations have been extensively reported in a number of articles and textbooks [2, 3, 6]. In this work, we only report a concise description of the operation system of a scanning integrated MZI (see **Figure 3(b)**).

In order to achieve good spectral resolution, the scanning Interferometer needs phase shifts suitable to produce interferograms of many tens of interference fringes. This involves the need that the substrate material has an electro-optical coefficient as high as possible. In our case, the output intensity is monitored as a function of the optical path variation induced by a suitable variable electric field, applied to the arms. The interferometric output I_{out} represents the Fourier Transform of the input spectral distribution $I(k)$ and is given by the following relationship:

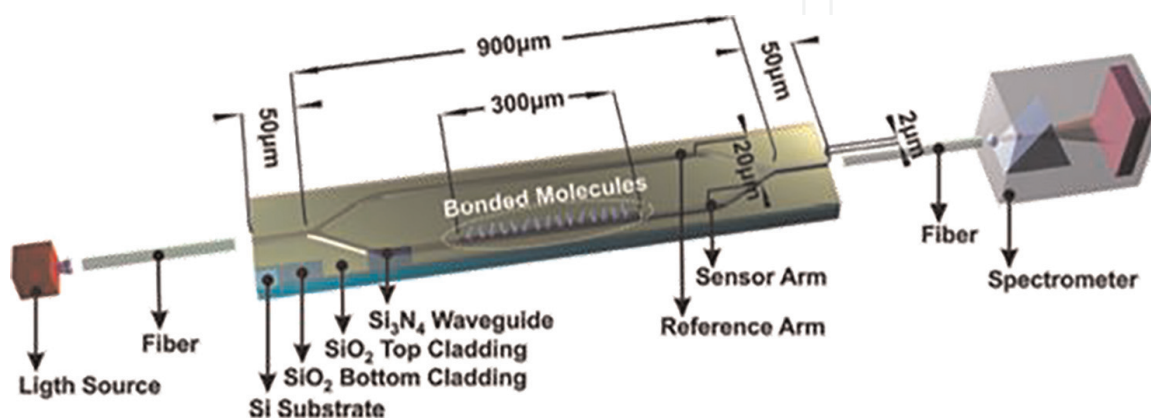


Figure 4. Hybrid MZI with a sensing pad in one arm integrated with a wavelength dispersive system [7].

$$I_{out}(\Delta p) = \int I(k) [1 + \cos(2\pi\Delta p(k))]dk, \quad (1)$$

where $k = 1/\lambda$ is the wavenumber of the incident radiation, and Δp is the optical path difference.

In our case, the optical path difference can be expressed by the linear relationship

$$\Delta p = L \Delta n, \quad (2)$$

where: L is the arm length, and

$$\Delta n = r_{33} \cdot n_e^3 \cdot E/2, \quad (3)$$

where r_{33} is the linear electro-optic coefficient along the optical c-axis, n_e is the LiNbO₃ extraordinary refractive index when x or y propagation is considered. Finally, E is the electric field applied to the driving electrodes.

From Eq. (1) it appears that in the case of monochromatic light, the intensities recorded by the detector, (i.e. the Interferogram), has a sinusoidal shape. In the real case, we deal with quasi-monochromatic light and the MZI output are somehow distorted as reported in **Figure 5** in the case of the incident light generated by a diode laser emitting in a narrow window around 635 nm.

When dealing with a wideband ('white') light, the conceptual behaviour is the same. Even if the interferogram is remarkably modified and several corrections must be applied to the over-simplified scheme previously reported [3], it is always possible to perform the spectrometric analysis of the incoming light. **Figure 6** reports an example of a real case of E131 dye (Patent Blue) detection with an integrated MZI.

More recently, a new generation of integrated architectures has been suggested for spectroscopic analyses, in particular the integrated monolithic version of the Young interferometer (YI) and the integrated monolithic version of the Michelson's ('Echelle') Diffractometer. **Figure 7** reports the sketch of the Young geometry in the integrated version. In this case, the waveguides' geometries are geometrically arranged like in the MZI, the only difference is at the detection side that is here based on an arrayed detector.

A more recent architecture has been realised on the basis of Michelson's echelle grating that, when fabricated with electro-optic material (LiNbO₃), becomes a Programmable Micro diffractive Grating (PMDG) extending the range of this kind of micro-optical device to an extremely large field of applications. **Figure 8** reports the

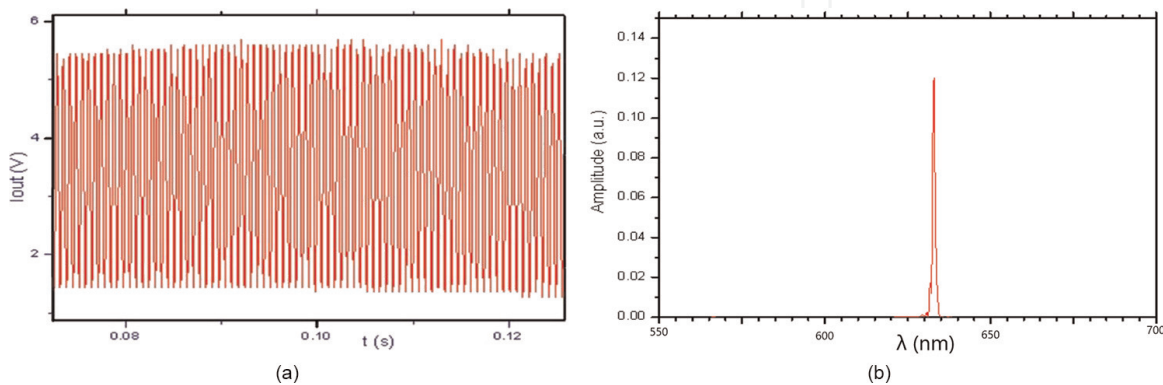


Figure 5. (a) Raw signal detected during the scanning cycle, (interferogram) and (b) the Fourier transform of the interferogram, giving the wavelength spectrum of the incident light.

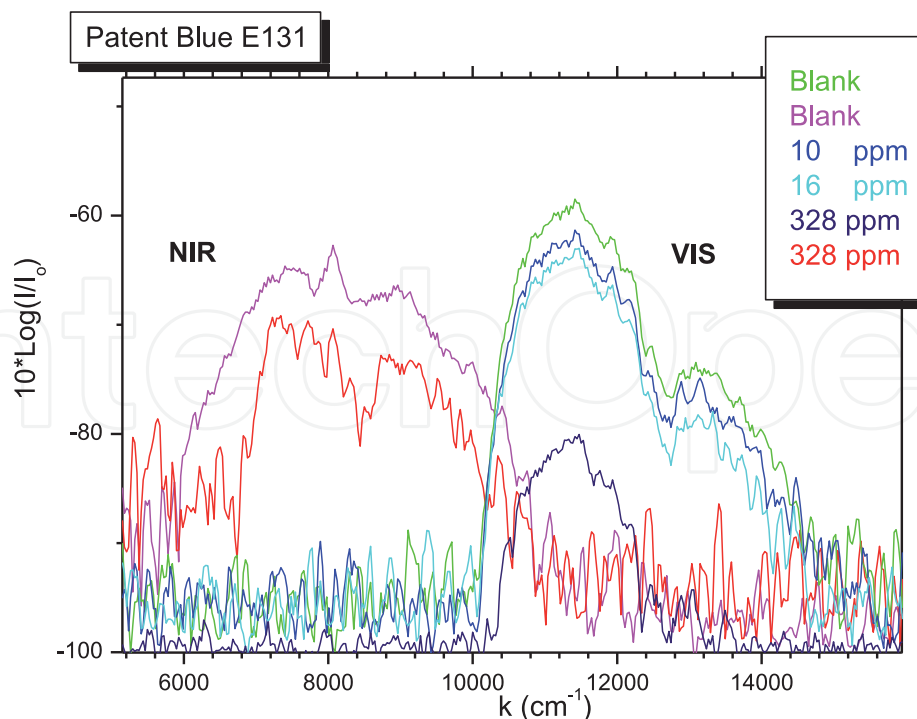


Figure 6.
Example of densitometry performed with an IO micro-interferometer on an E131 dye solution.

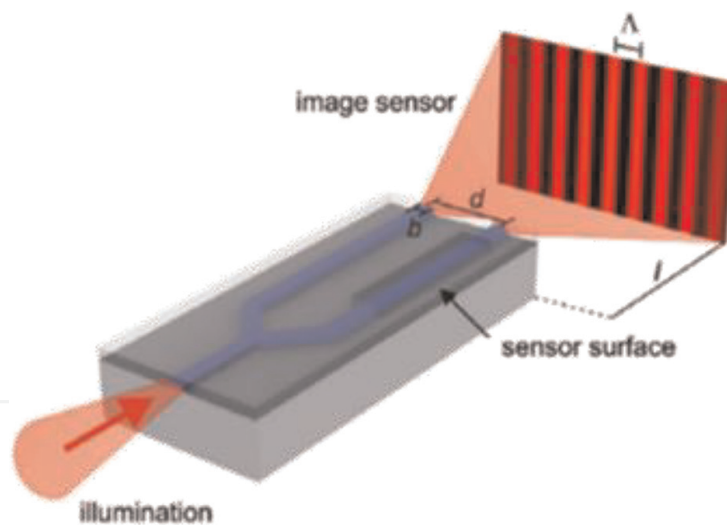


Figure 7.
Integrated version of the young interferometric geometry the far-field geometry for the detection of the modifications of the interference pattern, originated by the analyte adhesion on the sensing pad in one of the two arms.

comparison between the original static diffractive grating proposed by Michelson and the integrated PMDG, fabricated for high sensitivity detection systems based on the correlation spectroscopy technique. In Michelson's original device, the wavefront portions emerging from the different steps crosses different glass thicknesses, so the different optical paths acquire different phase shift as a function of the glass thickness crossed. The different wavefront emerging from each step interfere with each other giving rise to a far-field diffraction pattern that can be observed in far-field conditions on screen S, of **Figure 8(a)**.

If the integrated waveguides array sketched in **Figure 8(b)** is fabricated on electro-optical substrate, it can have the same behaviour as the Michelson's echelle device.

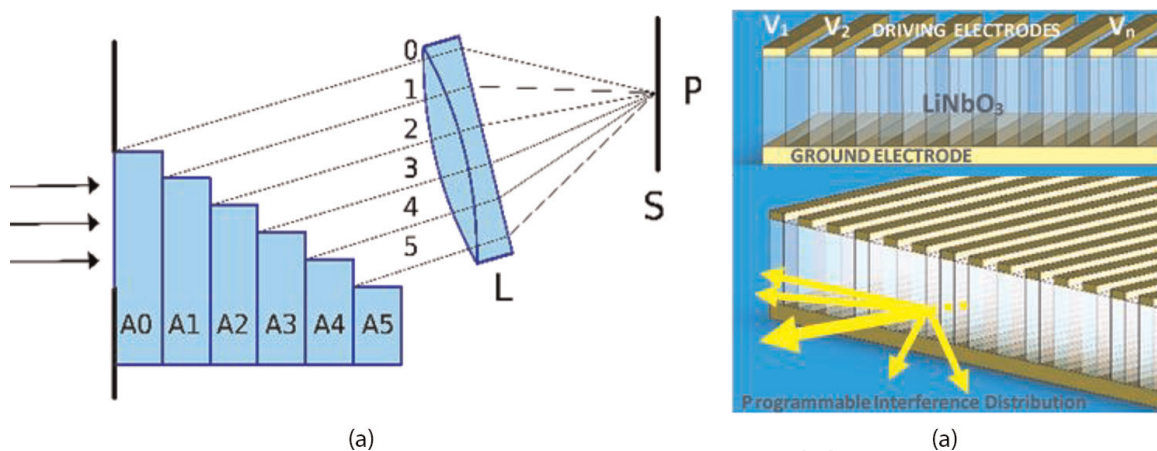


Figure 8. (a) Michelson's echelle diffraction grating. (b) Integrated programmable diffractive grating (PMDG) based on LiNbO_3 substrate.

In fact, each waveguide may have a different refractive index as a function of the electric field applied to the electrodes so, each portion of the wavefront emerging from each waveguide has a different phase and, in far-field conditions, they interfere with each other generating a diffraction pattern like in the case of Michelson's device.

The great difference between the two cases is that the device shown in **Figure 8(a)** is static and the diffractive properties are fixed by the construction parameters, whereas the PMDG device, the diffractive properties are programmable simply by changing the voltage applied at each electrode. This feature enormously expands the field of the applications of this Integrated Optics microdevice that can go far beyond the sensing systems arriving to have implications in many strategic areas such as optical fibre transmission, cryptography, quantum optic devices, optical computing, etc.

3.1 Holographic correlation spectroscopy with PMDG device

Correlation spectroscopy architectures have been widely studied for at least 20–30 years and are now argument described in the textbooks [8–10]. Therefore, in the present work, we will not enter in detail in the presentation of this technique and we will take as a reference the 'holographic correlation spectroscopy' architecture [11] treating in detail the subject of correlation spectroscopy in connection with the use of computer-generated optical elements. In particular, we will consider the conclusion of reference [11] when discussing the use of the PMDG to create synthetic spectra of several compounds, some of which are of interest for Environmental control, Food production and transportation, Bio-Chemical hazard, safety and security problems.

In particular, due to its programmability, the device can generate, at least in principle, synthetic spectra of almost any analyte of interest. The PMDG may have hundreds of diffractive elements in very small overall dimensions and, with the suitable software, it can generate a digital library containing the synthetic spectra of plenty of molecules. When the PMDG is exploited in this architecture, the sensing instrument described here can be considered as an example of a new sensor concept, in fact, in traditional instruments, the optical spectrum processing is determined by the correlation between the light transmitted through an unknown sample and the light transmitted through a reference cell containing a known mixture of the chemical molecule to be detected. In this case, due to the PMDG properties, the optical

spectrum processing is based only on the correlation between the light transmission through an unknown sample and the data of a digital library. This trait greatly increases the sensor flexibility if compared with other recent instruments in which the spectrally dispersed light is delivered onto a coded mask to provide spectral filtering of the sample spectrum light [11].

In conclusion, this new sensor is particularly suited for safety and security applications because it avoids the use of a reference cell containing reference materials that can be difficult and hazardous to handle, in the case of detection of dangerous, poisoning, or explosive targets. Furthermore, it allows great flexibility if compared with the coded mask filtering described in Ref. 11, because the number of molecules that can be detected is now only limited by the wavelength transmission window of the electro-optic material used as a substrate for the PMDG device and by the sensitivity range of the detector used. Finally, exploiting during the data collection the dark-field correlation technique, it can be obtained a remarkable increase in the sensitivity of the whole system. In fact, by using shrewdness to construct the reference synthetic spectrum to be the complement of the target transmission spectrum, the signal-to-noise ratio becomes very large. Actually, with this shrewdness, all the wavelengths different from those matching the absorbance of the target, are blocked creating a programmable filter that allows the transmission of only a very small fraction of the incident light in correspondence of the desired wavelengths exclusively. So, when the spectral absorption lines match the planned transmission complement it is obtained a very large signal-to-noise ratio, allowing extremely high sensitivity detection.

The architecture of ‘holographic correlation spectroscopy’ is schematically reproduced in **Figure 9**, is particularly simple and takes advantage of the intrinsic PMDG flexibility and reconfigurability features. In the geometry of **Figure 9**, a broadband ‘white’ light coming from an external source crosses, (one or several times), a sample cell containing the analyte to be investigated. Then the radiation crosses the PMDG optical element, placed in transmission architecture. In the present case, the external broadband light source could cover the whole transparency range of the LiNbO_3 base material ranging from $0.450 \mu\text{m}$ to $5.5 \mu\text{m}$.

The wideband radiation coming from the external source is then transmitted through the PMDG device and precisely defined by the ensemble of the programmed driving electrical potentials applied to the different waveguides. The degree of correlation between the sample cell spectrum, (unknown), and the synthetic spectrum

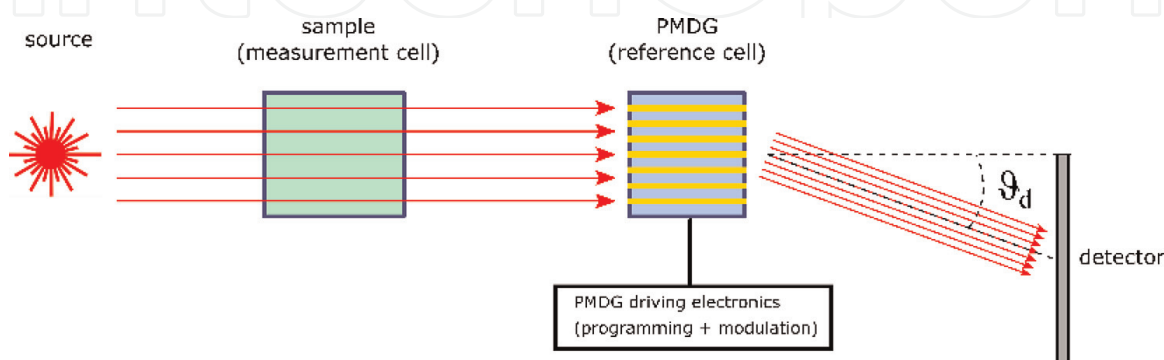


Figure 9. Schematic of a holographic correlation spectrometer set-up including the PMDG which acts as the reference cell. The light coming from a broadband source passes through the measurement cell which contains the unknown analyte. The diffraction pattern generated by the PMDG at the diffraction angle ϑ_d is perfectly matched to the spectrum of the target compound within the measurement cell.

programmed through the reference (PMDG) cell is then measured on a photodetector placed at a suitable diffraction angle ϑ_d .

To increase the sensitivity and the selectivity of the set-up, the usual techniques can be adopted, in particular: (i) Lock-in techniques are applied by modulating the transmission spectrum through the PMDG and recording the detector output at the same modulation frequency or/and (ii) Darkfield technique, i.e. applying a suitable map of the driving electrical potentials, the PMDG can be configured to synthesize the complement of the real target to be analysed, so obtaining a much larger signal-to-noise ratio and a consequent remarkable increase of both sensitivity and selectivity of the detection system.

3.2 Synthetic spectra generation mathematical approach

The key point in the programming of a waveguide-based PMDG for a synthetic spectra generation is the determination of a driving voltage pattern able to introduce the required phase shifts on each of the M waveguides, (Typically M can range from 50 to 200 waveguide/cm). In this way, the electromagnetic radiation emerging from the output face of the grating will generate the desired synthetic spectrum at a predetermined diffraction angle ϑ_d .

In this section, a mathematical framework for the specific case in which the functional elements are electro-optical waveguides is presented and discussed [12].

Under the hypothesis of working in the Fraunhofer approximation, the diffracted field at an angle ϑ_d , (see **Figure 9**) can be described by the following Fourier-transform integral:

$$U(\vartheta_d, \lambda) = \int_{-\infty}^{+\infty} \int_{\lambda_1}^{\lambda_2} \frac{CA}{\lambda} U'(x, \lambda) \exp\left(-\frac{i2\pi \sin(\vartheta_d)}{\lambda} x\right) d\lambda dx \quad (4)$$

where C is a constant of proportionality, A is the amplitude of the incident wave, supposed to be independent of the wavelength λ and x is the spatial transverse coordinate of the PMDG output facet whereas, λ_1 and λ_2 are the lower and upper limit of the spectral band of interest, respectively (**Figure 10**).

In Eq. (4), $U'(x, \lambda)$ is the near-field distribution emerging from the output facet of the PMDG. For a grating with M waveguides of width W and periodicity P , this distribution can be described by the following expression:

$$U'(x, \lambda) = \sum_{m=1}^M \exp\left(\left(-\frac{i2\pi L}{\lambda}\right)\left(\frac{Vm\gamma}{d}\right)\right) \exp\left(-\frac{(x - mP - P/2)^2}{\left(\frac{W}{2}\right)^2}\right) \quad (5)$$

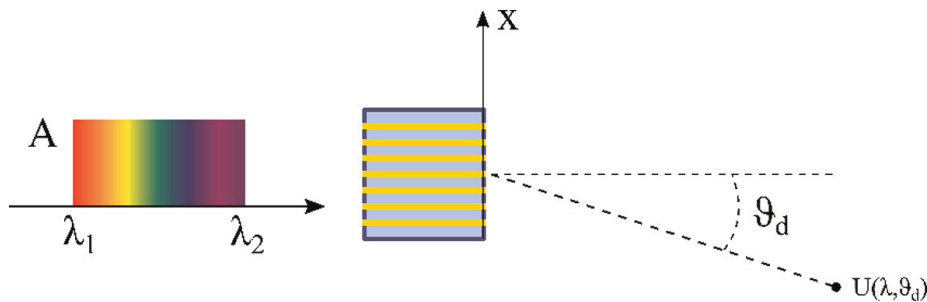


Figure 10.
Framework for the solution of the PMDG diffraction problem.

where L is the electrode length, d is the device thickness, V_m is the voltage applied to the m -th waveguide and γ is a constant depending both on the electro-optical characteristics and the crystallographic orientation of the substrate. In Eq. (5), the first exponential term of the summation describes the phase shift induced on the m -th waveguide by the local driving voltage V_m , whereas the second exponential term describes the mode profile emerging from each waveguide that, as a first approximation, is supposed to follow a Gaussian shape. Eq. (5) clearly shows how the local phase of the field emitted by the grating and, consequently, the diffracted pattern at angle ϑ_d , can be controlled through the application of a suitable set of M potentials $V_{m=1, \dots, M}$. The PMDG design and programming procedure is therefore reduced to the determination of a suitable voltage pattern, which minimises the difference between the target spectrum of interest and the synthetic one calculated with Eqs. (4) and (5). The difference between the target and the synthetic spectra can be quantified by introducing an error function \mathcal{E} of the form:

$$\mathcal{E} = \sqrt{\sum_{n=1}^N (I_n^d - I_n)^2} \quad (6)$$

where $I_n = |U(\lambda_n)|^2$ is the intensity of the target spectrum and I_n^d is the diffracted intensity spectrum at the considered diffraction angle ϑ_d , both evaluated over the same set of N wavelength within the spectral range of interest. Once this error function has been defined, the PMDG programming procedure reduces to the optimization problem of finding the minimum of \mathcal{E} with respect to the control parameters (V_1, V_2, \dots, V_M). By setting $K = L\gamma/d$ we can write, $D_m = K V_m$ and the new variables (D_1, D_2, \dots, D_M) have the dimension of a length, so each D_m value considers the optical path differences, the different waveguides.

This is physically equivalent to introducing a programmable phase-shift offset in the first term of Eq. (5). Then, the actual voltage pattern to apply to the different electrodes of the PMDG is calculated from the D_m values, resulting from the optimization routine, once the technological parameters have been defined.

For the solution of the multivariable optimization problem, several numerical approaches have been proposed and implemented so far, in particular, iterative Fourier Transform phase-retrieval algorithm [12], genetic algorithms [11] or gradient-based multi-variable minimization routines [13]. The Nelder–Mead Simplex Method [14] demonstrates to be extremely effective providing a monotonic and rapid convergence to the minimum of the error function \mathcal{E} . Moreover, the numerical implementation of this method is available in the most common scientific computation libraries.

An example of synthetic spectrum created with the numerical method of reference [14] is reported in **Figure 11** where a portion of the COCl_2 spectrum has been reconstructed in the hypothesis of a PMDG having $M = 50$ waveguides $W = 8 \mu\text{m}$ and pitch $P = 80 \mu\text{m}$. The experimental absorbance spectrum is shown in **Figure 11(a)**, whereas the calculated synthetic one at the optimal diffraction angle ϑ_d of 3.75 degrees is presented in the (b) panel of the same Figure. The (c) panel shows the optimised parameters set D_m calculated with the numerical routine that, once introduced in (2), generates the synthetic spectrum displayed in (b). The agreement between the two spectra is remarkable over the entire wavelength range of interest, confirming both the effectiveness of the PMDG device and of the numerical optimization routine adopted to retrieve the programming pattern.

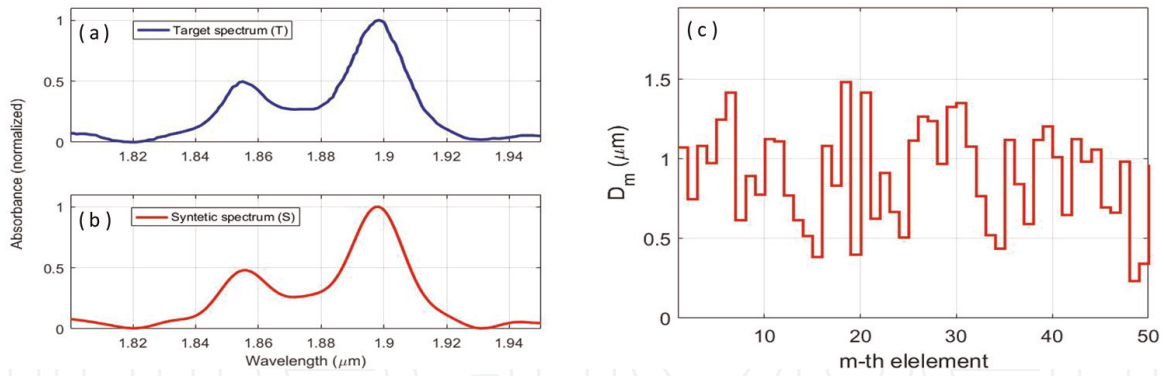


Figure 11. (a) Experimental absorbance spectrum of gaseous phosgene (target spectrum T) and (b) PMDG-synthesized spectrum of the same analyte (synthetic spectrum S). (c) Values of the optimised D_m ($m = 1..50$) control parameters.

4. Integrated interferometers for ghost imaging in the spectral domain

The Ghost Imaging, (GI) phenomenon is based on the spatial correlation of light to form images and, since the early pioneering work in 1995, several experiments on the argument have been presented [15–18]. The GI is obtained by correlating the intensities of two spatially separate light beams, one of the two light beams illuminates an object to be imaged. The second beam, which does not see the object, (reference beam), if it is detected with a position-sensitive sensor, gives rise to the spatial image of the object created by the non-interfering photons.

Besides the GI in the space domain, another kind of ‘ghost experiments’ were performed in the frequency (Spectral), domain [19–21]. It must be pointed out that in Ref. to [20], these kinds of experiments were performed using a classical thermal light emitted by a broad-band superluminescent diode. These experiments allowed to exploit real spectroscopy measurements detecting spectral lines of chemical molecules like CHCl_3 [20] and the spectral lines of Er^{3+} dopant [21] in LiNbO_3 non-linear material placed in one arm of an Asymmetric Non-Linear Interferometer, (ANLI). These preliminary approaches to experimental spectroscopic sensing demonstrate that a new field of sensing can be opened exploiting effects such as ‘ghost spectrometry’. These new sensing techniques can allow extending the sensing limits of the traditional detectors and performing spectrometric measurements with non-interacting photons.

Before describing the experimental procedures, of ghost imaging in the frequency domain, let us give a rapid oversimplified description of the basic principles of the ‘ghost’ phenomena. In Ref. [22], this architecture was studied in detail and it was concluded that it gives rise to a condition that is often referred to as maximally entangled states of a two-mode field. If the two modes are physically separated like in the case of the arms of an MZI, we are in presence of separate path-entangled states that can have important applications to interferometry and interferometric analyses.

In particular, considering the case of a coherent intense light beam injected in an integrated MZI, the photons are spatially confined in geometrically separated single-mode waveguides, where they have a very high spatial and time coherence [22]. Moreover, the photon density inside the waveguides can reach values that are orders of magnitude higher than in the case of free space propagation. In these conditions, an integrated optical device is particularly suitable for both practical applications and basic quantum optics studies.

The integrated version of an ANLI, used to obtain ghost imaging in the frequency domain [23], is schematically reported in **Figure 12** as taken from reference [21].

In that case, the ANLI was not built as a monolithic device but was realised in a hybrid set-up in which the 980 nm Laser source was injected in a 50:50 Y coupler single-mode optical fibres. One arm was coupled with an Er³⁺ doped LiNbO₃ monolithic waveguide, whereas the other arm was coupled with a monolithic Pockels phase modulator as the one shown in **Figure 2**. Then the MZI geometry was completed by coupling the two arms with an identical second optical fibre Y coupler. Finally, the injected 980 nm photons arrive in the photodetector passing through a (975 ± 25) nm pass-band filter that eliminates all the photons generated by the interaction of the 980 nm pump with the Er³⁺ doped nonlinear LiNbO₃ arm. In any case, the photons generated by the interaction in the doped arm can only give rise to a continuous background because they cannot contribute to the interference process due to the ‘Which Way’ criterion.

The principle of the experiment was based on the Quantum properties stating that two Fourier Transform pairs are conjugate variables. So, operating a Fourier Transform in the time-frequency space-domain, it is possible to get information on the wavenumber space-domain of the 930 nm pump photons annihilated, (generating up or down-conversion), as a consequence of the pump photons interaction with the Er³⁺ doped nonlinear LiNbO₃. This intriguing effect takes place when the doped material is placed in one arm of the ANLI and the photodetector do not even see the photons generated by up or down-conversion in the doped arm.

The spectroscopy experiment was performed by injecting the 980 nm laser beam in the input port ‘a’ of **Figure 12**. A fraction of the pump 980 nm photons is absorbed by the Er³⁺ dopant, giving rise to a series of up and down conversions having a widely studied spectral composition as reported in literature. Then, a linear voltage ramp is applied to the undoped arm of the ANLI producing a continuous phase shift variation between the photonic states entangled over the two optical paths of the ANLI. The pass-band filter ensured that only the 980 nm pump photons could reach the detector. The experimental data were collected detecting the intensity of transmitted photons as a function of time (i.e. of the phase shift), giving rise to the raw interferograms

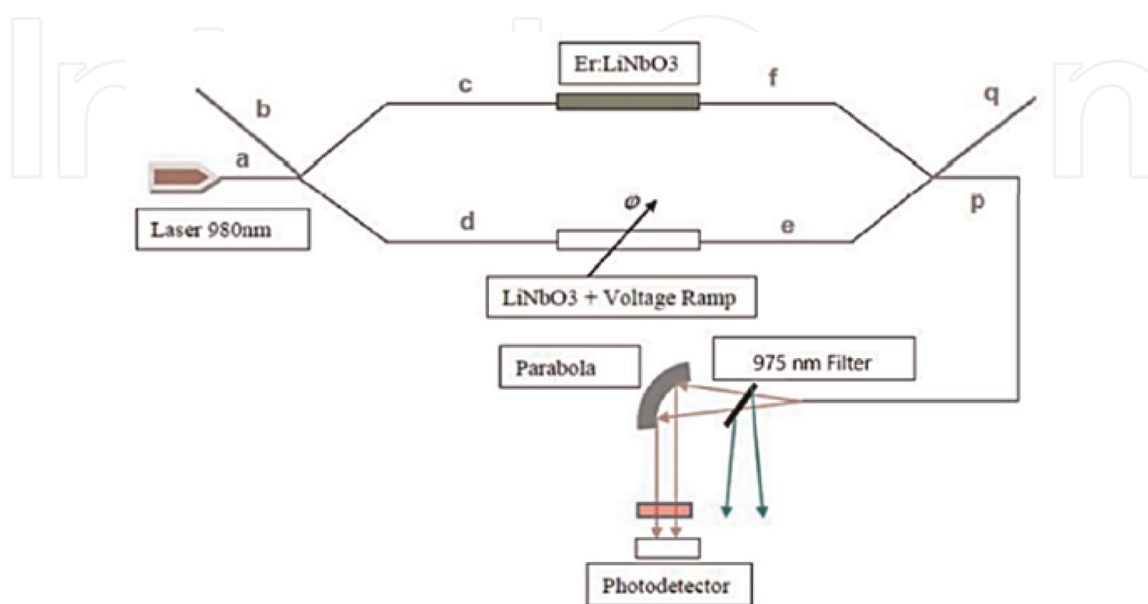


Figure 12. Schematic of the experimental layout. The ANLI is used in [21].

shown in the inserts of **Figure 13(a)** and **(b)**. Then, the raw interferograms were elaborated by the usual methods used in Fourier Transform Spectroscopy [18, 24]. The same measurement was first performed by using an InGaAs photodetector having a detectability window extending up to wavelengths of 2.5 μm (in the SWIR region). The measurement was then repeated using a Si p-i-n detector that is 'blind' at wavelengths $\lambda \geq 1.1 \mu\text{m}$. The results of the two experiments are reported in **Figure 13(a)** and **(b)**, respectively.

In **Figure 13**, the two spectroscopic measurements of the Er^{3+} energy levels performed with an InGaAs p-i-n photodetector, (**Figure 13(a)**) and with a Si p-i-n photodetector, (**Figure 13(b)**) are comparatively reported.

The complete Er^{3+} Spectrum extending from visible to SWIR wavelengths was obtained reporting most of the spectral lines as listed in the literature.

The difference in the amplitudes can be attributed to the different sensitivities of the two detectors. Moreover, as previously clarified, only the 980 nm monochromatic pump photons that have not interacted with the Er^{3+} doped crystal can reach the detector. In fact, the 980 nm photons that interacted with Er^{3+} are annihilated, giving rise to the up or down-conversion photons that are eliminated by the (975 ± 25) nm passband filter.

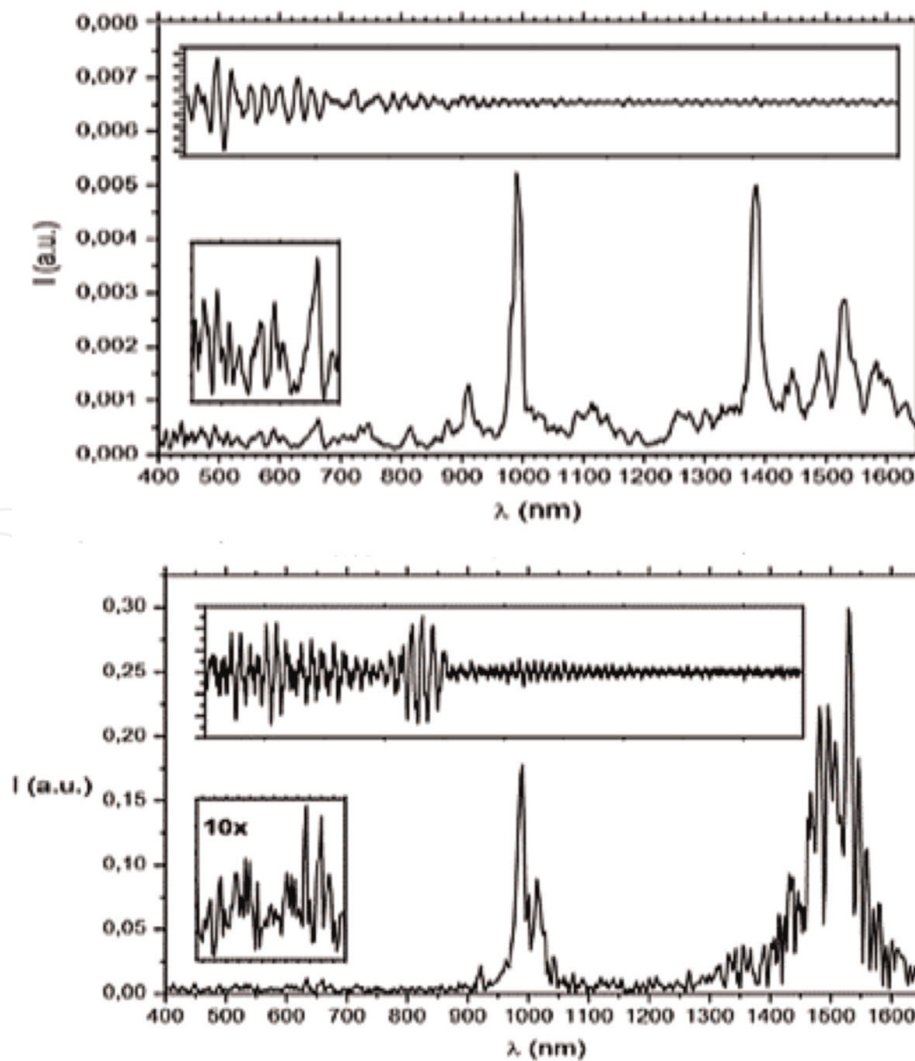


Figure 13. Spectra obtained by Fourier transform analyses with the setup of **Figure 12** (see text).

In conclusion, with the ANLI integrated architecture reported in **Figure 12**, the Er^{3+} spectral lines appeared independently of the different sensitivity of the used detectors also over the whole SWIR, where the Si *p-i-n* detector is ‘blind’. Considering that, due to the passband filter, only the non-interacting monochromatic photons have reached the detectors, we can say that the Er^{3+} spectral lines are ‘ghost’ lines produced by the separate path entangled states correlation [22] generated in the two arms of the interferometer.

The previously described results give a strong indication that, by using ‘ghost imaging’ in the frequency domain, it is possible to develop a new generation of integrated interferometric instruments, (most likely based on the ANLI architecture of **Figure 12**), having the capability to work with interaction-free photons. This allows extending the spectral measurement remarkably beyond the photodetector sensitivity limits, in particular in spectral regions where the photodetectors are not available or have too low sensitivity. In particular, some preliminary contacts indicate that this effect is of strong interest for several applications, with particular attention to astrophysical applications.

5. Integrated optics interferometry for astrophysics

5.1 Stellar interferometry with integrated optics

Optical long baseline interferometry is a technique that is undoubtedly providing high angular resolution observations in optical astrophysics. Fizeau in 1868 [25] was the first to attempt using interferometry for astronomical observations, without reaching the wanted result, eventually proposed and revised by Stéphane in 1874 [26]. Nevertheless, only in 1921, Michelson and Pease [27] first succeeded in measuring stellar diameters with a single telescope equipped with a pupil mask. The schematics and characteristics of their apparatus are reported in **Figure 14**. Unfortunately, their interferometer was not that sensitive to allow further investigation. In fact, a 1.0 milliarcsecond diameter on the sky translates to $0.5 \mu\text{m}$ in optical path difference (OPD), on a $B = 100 \text{ m}$ baseline (see **Figure 14**).

In practice, modern direct interferometry only started in 1975 with Labeyrie [28] who produced stellar interference with two separated telescopes.

Modern long baseline interferometry requires the combination of several stellar beams collected from different apertures (telescopes). The first interferometers started working with only two apertures, such as GI2T [29], SUSI [30], PTI [31], IOTA [32], COAST [33] and NPOI [34, 35]. The increase in the number of apertures was one of the major features of new generation interferometers. Today, the principal operational interferometric observatories, which use this type of instrumentation, include VLTI [35–45], and CHARA [37].

Current projects are using interferometers to search for extrasolar planets, either with nulling techniques, by astrometric measurements of the reciprocal motion of the star or through direct imaging.

In **Figure 15**, the geometry of the ideal interferometer is reported. Let us specify the incident source flux power F in units of energy incident per unit time per unit cross-sectional area, and the collecting area of the apertures A_1 and A_2 as A . Then, apart from some efficiency factors, the detected power P expresses as per the following:

$$P = 2AF (1 + \cos k(s B + d_1 d_2)), \quad (7)$$

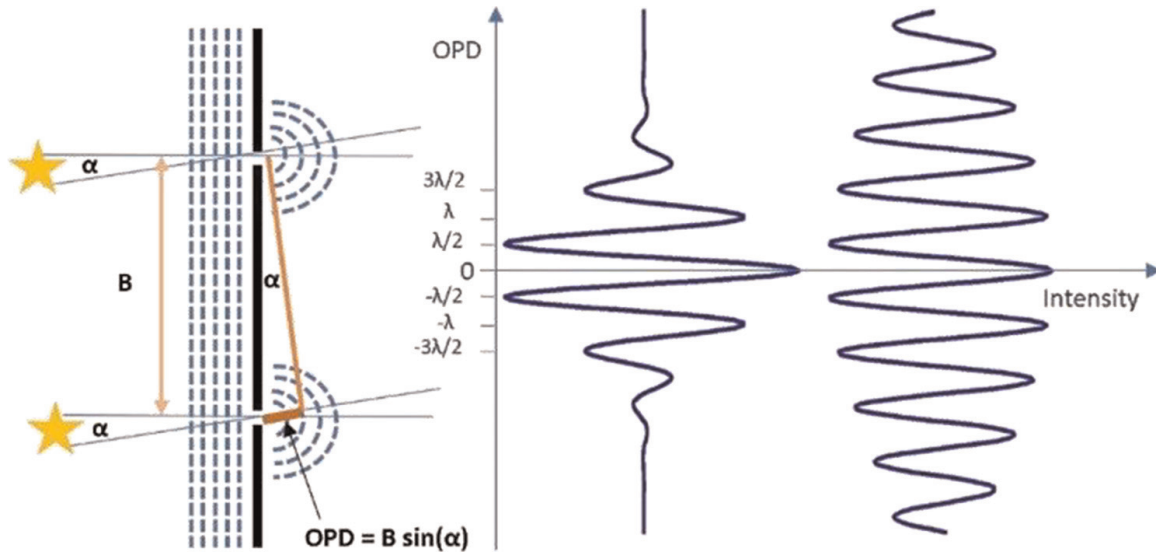


Figure 14.

(a) Scheme of the two slits mask experiment from Michelson and Pease. A star, with an α angular diameter, is imaged after its light passes through a double slit mask, with B as the slit distance. An interferogram appears as a function of the optical path difference (OPD), with the first minimum at $OPD = \lambda/2$, where λ is the wavelength of the impinging light. The fringes disappear when the OPD overcomes the source coherence length, e.g. (b) and (c) show different coherence length interferograms.

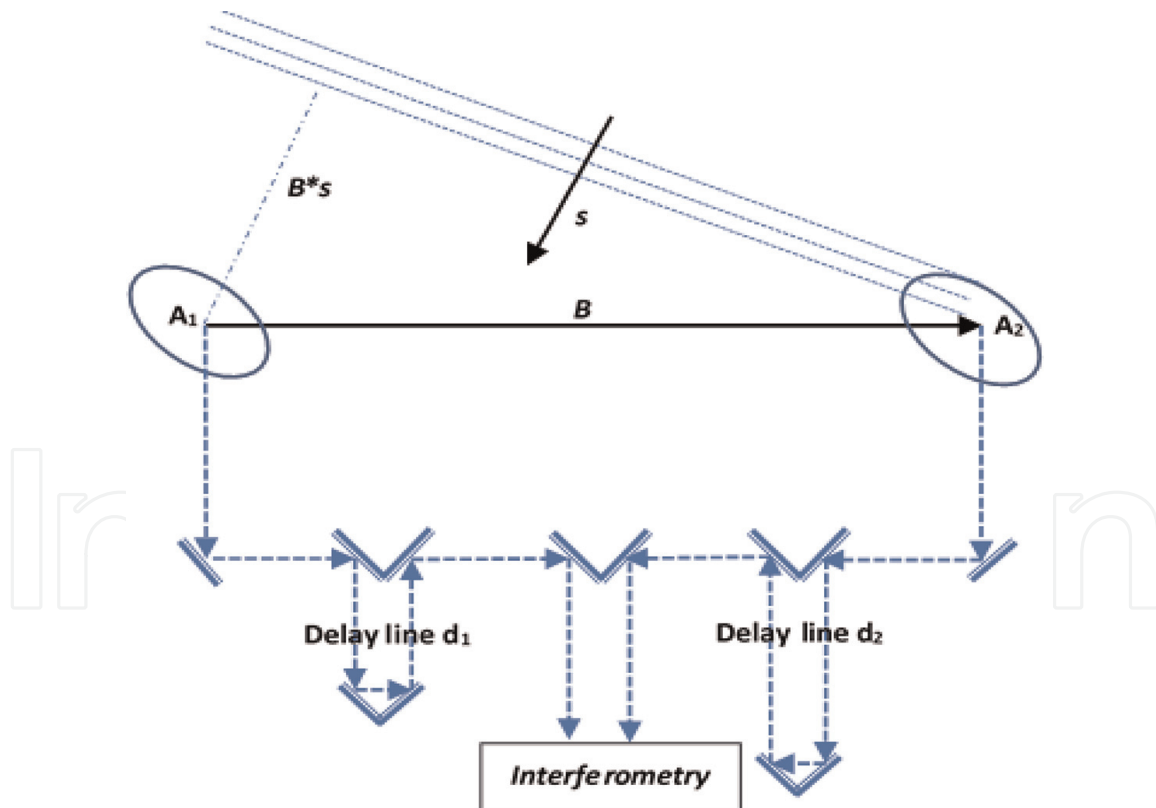


Figure 15.

Ideal stellar interferometer schematics.

where $k = 2\pi/\lambda$, \mathbf{s} is the unit vector normal to wavefront propagation and \mathbf{B} is the baseline vector between the two apertures.

In the space of relative delay $D = \mathbf{s} \cdot \mathbf{B} + \mathbf{d}_1 \cdot \mathbf{d}_2$, P varies harmonically between zero and $2AF$ with period λ . It is important to recall that for conventional imaging, the limiting angular resolution α follows the well-known relationship $\alpha \sim \lambda/D$, (where D is

the telescope pupil diameter and λ is the wavelength), therefore, in comparison, an interferometric system provides the measure of interference fringes between two beams at higher angular frequencies, in the order of $\alpha \sim \lambda/B$.

The complex visibility of these fringes is proportional to the Fourier transform of the object intensity distribution (Van-Cittert Zernike theorem), hence allowing to resolve particulars, very narrow from the angular point of view. Following these principles, stellar interferometry is offering to present days astronomers the ability to study celestial objects in unprecedented detail. It is possible to see details on the surfaces of stars and even to study celestial bodies close to a black hole [46] (**Figure 16**).

Stellar interferometry has become even more effective due to the advent of high sensitivity detectors and of large aperture telescopes. Nevertheless, to implement it, a complex system of mirrors has normally to be set up to bring the light from the different telescopes, constituting the synthetic aperture, to the instruments, where it is combined and processed (see scheme in **Figure 17**). This is technically demanding,

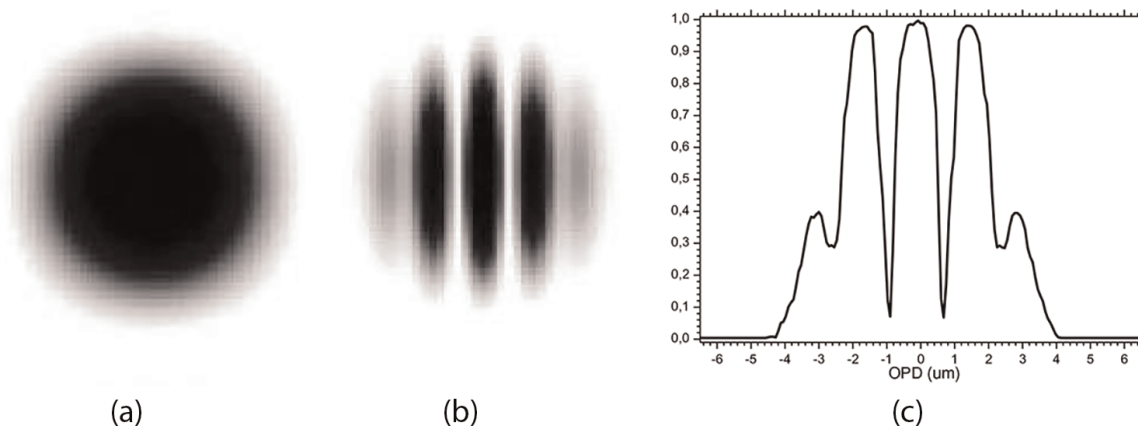


Figure 16.
 (a) Conventional star image, (b) same with two telescopes stellar interferometry having baseline $B = 10D$, and, (c) corresponding interference pattern profile.

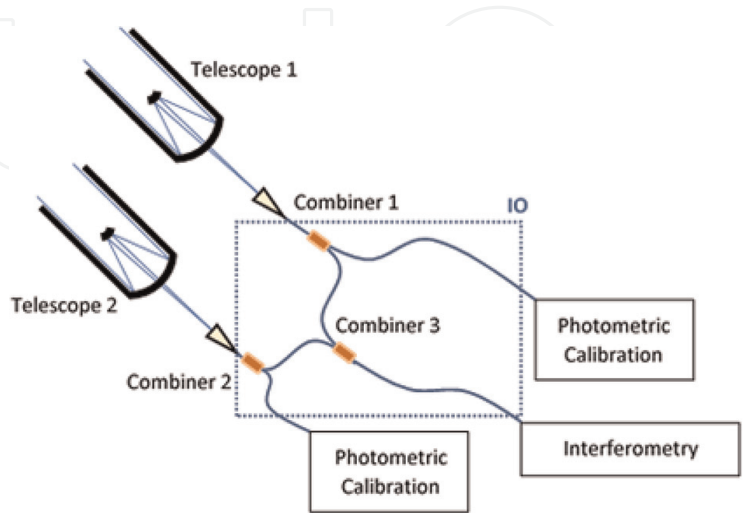


Figure 17.
 Schematics of IO apparatus required for two telescopes stellar interferometry. Light from the same source collected by telescopes 1 and 2 is injected in 2x2 IO beam splitters/combiners 1 and 2, respectively. One output port of each combiner is used to perform photometric adjustment whereas the second ports are combined in a third IO 2x2 beam splitter/combiner, at which output ports the interferometric signal is collected and processed.

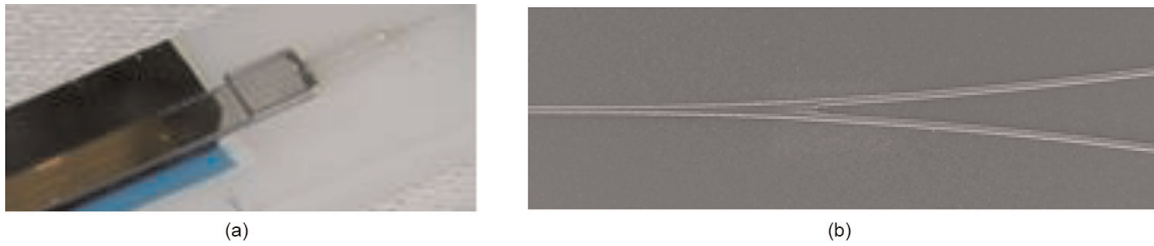


Figure 18. (a) Fibre pig-tailed IO y-branch mounted on mechanical support, (b) SEM picture of the IO Y-junction, allowing beam splitting as well as fibre signal combining.

as the light paths have to be set equal to within $1.0 \mu\text{m}$ over distances of a few hundred metres, in order to avoid an OPD offset out of the coherence length.

For ground-based interferometers, the source phase is corrupted by atmospheric turbulence. This prevents an absolute measurement of the source phase. However, it is possible to measure the difference in the source phase between two wavelengths. In practice, stellar interferometry requires star tracking techniques to compensate for astronomic seeing due to atmospheric turbulence.

In recent years, integrated optics and photonics technology, inherited from the telecom field and micro-sensor applications, was proposed for astrophysical interferometry. Results obtained with components coming from micro-sensor application were first presented by Berger et al. in a seminal series of dedicated works [38–44]. These authors demonstrated the validity and feasibility of the integrated optics technology for astronomical interferometry, by using telecom fibre coupler/combiners. Following a complete laboratory characterisation of the optical properties of the applied IO components, a first set-up was tested at the Infrared Optical Telescope Array (IOTA) observatory, in Arizona.

The above-mentioned studies demonstrated that beam combiners are very stable and lead to precise measurements. Moreover, IO components are versatile and easy to handle. In particular, the number of optical alignment adjustments strongly simplifies, which dramatically reduces the complexity of multiple-beam combinations for aperture synthesis imaging (**Figure 18**).

Other examples of IO based stellar interferometers are present by the VLTI, where the VINCI apparatus, based on IO beam combiners and fibre optics components, has allowed astronomers to reach the unprecedented resolution of 4.0 milliarcseconds in sky observations [46].

5.2 IO Mach-Zehnder micro-interferometers for earth and space remote sensing

Absorption or emission spectroscopy is largely adopted for remote sensing in both Earth and Space exploration, on board dedicated satellite platforms.

In this case, all general resources (weight, encumbrance, energy consumption, etc.) are particularly limited, furthermore, the onboard instrumentation is exposed to harsh environmental conditions (vibrations, ultra-high vacuum, radiation, temperature gradients, etc.). For these reasons, IO devices can represent a very important solution, particularly when based on monolithic structures (**Figure 19**).

Integrated scanning micro-interferometers with Mach-Zehnder geometry, have been designed and produced by using MEOS (Micro Electro Optical Systems) technologies.

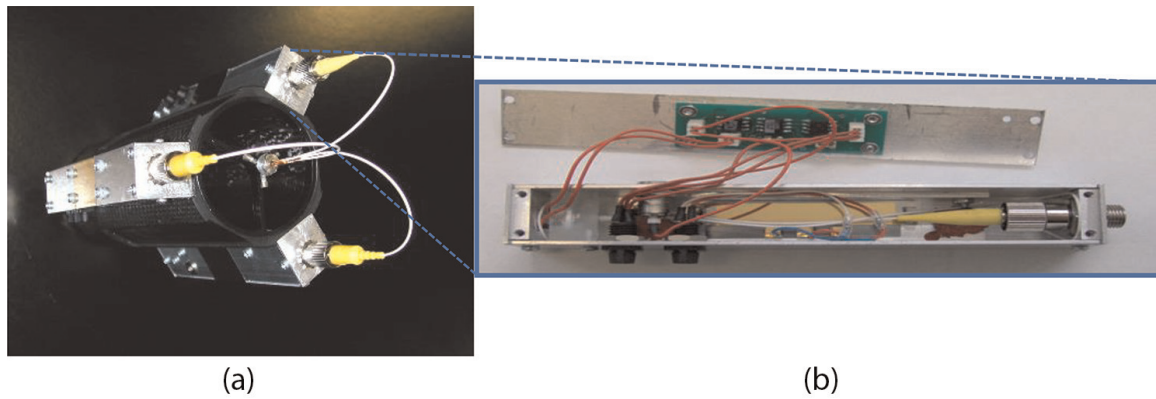


Figure 19. (a) Carbon fibre telescope integrating three IO micro-interferometers. (b) Detail of an integrated MZ micro-interferometer equipped with front-end optics, readout electronics and packaging, ready to use (the overall package length is 12 cm).

The obtained micro-devices are based on integrated optical waveguides on LiNbO_3 (LN) crystals, electrically driven, without moving parts, by exploiting the electro-optical properties of the material. These IO devices are Fourier Spectrometers in that they operate the Fourier Transform of the input radiation spectral distribution, which is eventually recovered starting from the output signal by means of Fast Fourier Transform (FFT) techniques.

Such micro-interferometers weigh a few grams, require a power consumption of a few mW and, in principle, can operate in the whole LN transmittance range ($0.36 \mu\text{m}$ – $4.5 \mu\text{m}$).

In the literature several works have been reported [12, 47, 48] describing the development of a whole series of micro-interferometric apparatuses, demonstrating in principle the applicability of IO MEOS technology for Space exploration and Earth remote sensing. The micro-interferometers were produced on x-cut LiNbO_3 single-crystal substrates, by applying non-conventional micromachining techniques, based on high-energy particle beams processing.

Performances were particularly tested in the $0.4 \mu\text{m}$ – $2.5 \mu\text{m}$ spectral window, with some extension also in the $2.5 \mu\text{m}$ – $4.5 \mu\text{m}$ range. In the Visible region $0.4 \mu\text{m}$ – $0.7 \mu\text{m}$ this microsystem demonstrated a spectral resolution suitable for detecting the

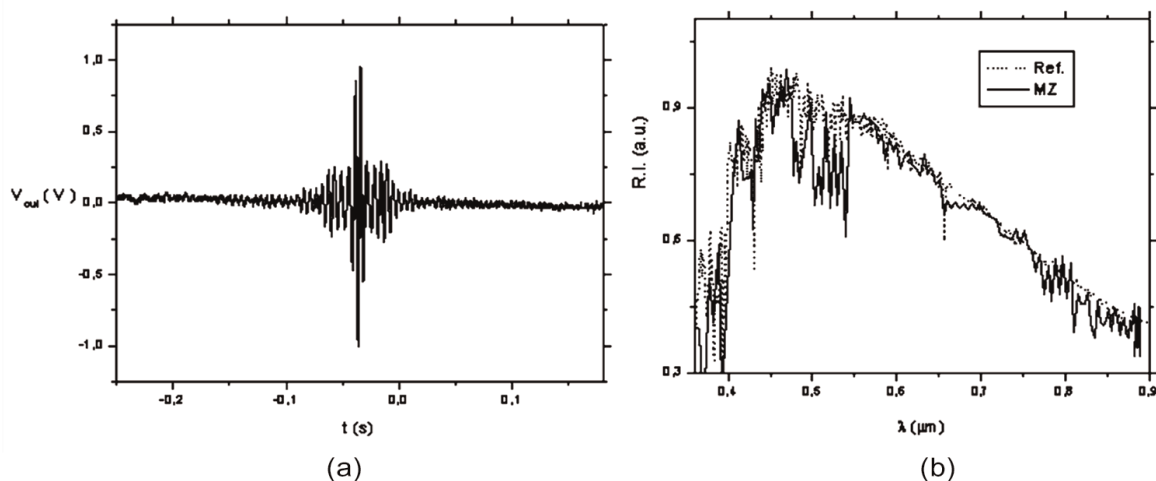


Figure 20. (a) Solar radiation interferogram, (b) corresponding FFT (solid), reference (dot).

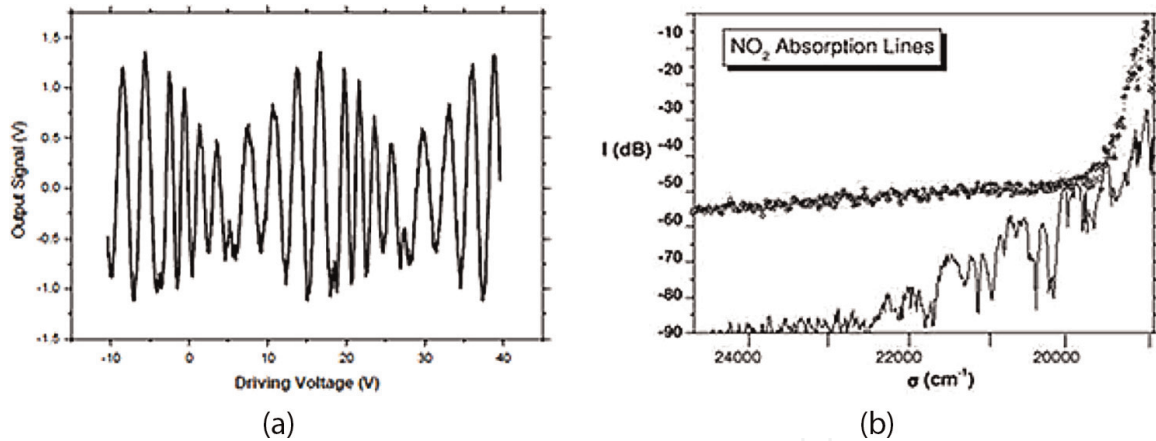


Figure 21.

(a) Raw interferogram as obtained from an integrated scanning MZI, and (b) the absorption analysis of the NO₂ analyte, (lower curve), introduced in a wide band light (upper curve).

characteristic lines of the solar spectrum together with the absorption bands of common gases present in Earth's atmosphere (see **Figures 20** and **21**).

6. Conclusions

Recent developments of Integrated Optics and Photonics components allow implementing complex, rugged, robust and miniaturised interferometric systems, which applications span all the fields of sensing interferometry also including the possibility of upcoming quantum effects applications, already shortly mentioned in paragraph 4. In this work, a general overview of the present state of the art was presented, with the intention to stimulate the interests of investigators and researchers operating in multidisciplinary contexts and in general in all fields of sensing and analytics.

Author details


Marco Chiarini^{1*}, Alberto Parini¹ and Gian Giuseppe Bentini^{1,2}

1 Prometheus Srl, c/o CNR-IMM, The Italian National Research Council, Institute for Microelectronics and Microsystems, Bologna, Italy

2 CNR-IMM, The Italian National Research Council, Institute for Microelectronics and Microsystems, Bologna, Italy

*Address all correspondence to: chiarini@bo.imm.cnr.it

IntechOpen

© 2022 The Author(s). Licensee IntechOpen. This chapter is distributed under the terms of the Creative Commons Attribution License (<http://creativecommons.org/licenses/by/3.0>), which permits unrestricted use, distribution, and reproduction in any medium, provided the original work is properly cited. 

References

- [1] Kozna P et al. Integrated planar optical waveguide interferometer biosensors: A comparative review. *Biosensors and Bioelectronics*. 2014;**58**:287-307. DOI: 10.1016/j.bios.2014.02.049
- [2] Born M, Wolf E. *Principles of Optics*. Cambridge, UK: Cambridge University Press; 1999. DOI: 10.1017/CBO9781139644181
- [3] Fritzsche W, Popp J. *Optical Nano- and Microsystems for Bioanalytics in Springer Series on Chemical Sensors and Biosensors*. Germany: Springer Verlag Berlin Heidelberg; 2012. pp. 103-154. DOI: 10.1007/978-3-642-25498-7_4
- [4] Kuntz RE. Miniature integrated optical modules for chemical and biochemical sensing. *Sens. & Actuat.* 1997;**B38**:13-28. DOI: 10.1016/S0925-4005(97)80167-0
- [5] Heideman RG et al. Performance of a highly sensitive optical waveguide Mach-Zehnder interferometer immunosensor. *Sens. & Actuat.* 1993;**B10**:209-217. DOI: 10.1016/0925-4005(93)87008-D
- [6] Kitsara M et al. Broadband Mach-Zehnder interferometry as a detection principle for label-free biochemical sensing. In: *SENSORS Proceedings*; 26–29 October 2008; Lecce, Italy: IEEE; 2008. pp. 934-937. DOI: 10.1109/ICSENS.2008.4716594
- [7] Wilson J, Hawkes J. *Optoelectronics: An Introduction*. Prentice Hall NJ; 1998
- [8] Zhou G et al. Design of the diffractive optical elements for synthetic spectra. *Optics Express*. 2003;**11**:1392-1399. DOI: 10.1364/OE.11.001392
- [9] Sinclair MB et al. *Correlation Spectrometer*. 2010. U.S. Patent 7 697 134 B1
- [10] Smith MW et al. Theoretical description and numerical simulations of a simplified Hadamard transform imaging spectrometer. In: *Proceedings of International Symposium on Optical Science and Technology*, 8 November 2002. Vol. 4816. Seattle, WA, United States: SPIE; 2002. pp. 372-380. DOI: 10.1117/12.451698
- [11] Basti G et al. Sensor for security and safety applications based on a fully integrated monolithic electro-optic programmable micro diffracting device. In: *Proceedings SPIE Security + Defence*, 2019, Strasbourg, France. *Electro-Optical and Infrared Systems: Technology and Applications XVI*. Vol. 11159. Strasbourg, France; 2019. p. 1115907. DOI: 10.1117/12.2532107
- [12] Bentini GG et al. Fully integrated Mach-Zehnder Microinterferometer on Lithium Niobate as an example of Micro electro Optical system for space applications. In *5th ESA round table on micro/nano technologies for space*, Norwijk, The Netherlands, 2-5 October 2005. Available on line: <http://www.cong rex.nl/05c12>
- [13] Sinclair MB. Synthetic spectra: A tool for correlation spectroscopy. *Applied Optics*. 1997;**36**:3342-3348. DOI: 10.1364/ao.36.003342
- [14] Bentini GG et al. Monolithic fully integrated programmable microdiffraction grating based on electro-optical materials. In: *Proceedings of Proc., Photonic Materials, Devices, and Applications II*, 12 June 2007. Maspalomas, Spain: SPIE; 2007. pp. 6593-659325. DOI: 10.1117/12.724171
- [15] Pittman TB et al. Optical imaging by means of two-photons quantum entanglement. *Physical Review A*. 1995;

52(5):R3429-R3432. DOI: 10.1103/PhysRevA.52.R3429

[16] Markie D, van Voorthuysen EH. Realization of an interaction-free measurement of the presence of an object in a light beam. *Am. J. of Phys.* 1996;**64**:1504-1507. DOI: 10.1119/1.18413

[17] Barreto Lemos G et al. Quantum imaging with undetected photons. *Nat. Lett.* 2014;**412**:409-412. DOI: 10.1038/nature13586

[18] Amiot C et al. Supercontinuum Spectral-domain ghost imaging. *Optics Letters.* 2018;**43**(20):5025-5028. DOI: 10.1364/OL.43.005025

[19] Scarcelli G et al. Remote spectral measurements using entangled photons. *Applied Physics Letters.* 2003;**83**:5560-5562. DOI: 10.1063/1.1637131

[20] Janassek P et al. Ghost spectroscopy with classical thermal light emitted by a superluminescent diode. *Phys. Rev. Applied.* 2018;**9**:021001-1-021001-4. DOI: 10.1103/PhysRevApplied.9.021001

[21] Chiarini M et al. Theoretic approach to ghost imaging in the frequency domain performed by means of a high brilliance coherent monochromatic source. In: *Proceedings of SPIE Security + Defence, 2019, Strasbourg, France SPIE (2019) 11159, Electro-Optical and Infrared Systems: Technology and Applications XVI.* 1115905. Strasbourg, France. DOI: 10.1117/12.2532307. Available from: <https://www.spiedigitallibrary.org/conference-proceedings-of-spie/browse/SPIE-Security-Defence/2019>

[22] Gerry CC et al. Nonlinear interferometer as a resource for maximally entangled photonic states: Application to interferometry. *Physical Review A.* 2002;**66**:013804. DOI: 10.1103/PhysRevA.66.013804

[23] Chiarini M et al. Spectroscopy of non interfering photons through a non-linear integrated optics Mach-Zehnder interferometer. In: *Proceedings of Optics + Optoelectronics, 2017, Prague. Czech Republic. SPIE.* 2017;**10230**:1023004-1023003. DOI: 10.1117/12.2265742

[24] Li J et al. Miniature Fourier transform spectrometer based on wavelength dependence of half-wave voltage of a LiNbO₃ waveguide interferometer. *Optics Letters.* 2014;**39**:3923-3926. DOI: 10.1364/OL.39.003923

[25] Fizeau H. *C. R. Acad. Sci. Paris.* 1868;**66**:932. DOI: N/A

[26] Stéphan E. *C. R. Acad. Sci. Paris.* 1878;**78**:1008. DOI: N/A

[27] Michelson AA, Pease FG. *The Astrophysical Journal.* 1921;**53**:249. DOI: N/A

[28] Labeyrie A. *The Astrophysical Journal.* 1975;**196**:L71-L75. DOI: N/A

[29] Mourard D et al. The GI2T interferometer on plateau de Calern. *A&A.* 1994;**283**(2):705-713. DOI: N/A

[30] Davis J et al. The Sydney university stellar interferometer -II. Commissioning observations and results. *Month. N. of the Royal Astr. Soc.* 1999;**303**(4):783-791. DOI: 10.1046/j.1365-8711.1999.02270.x

[31] Colavita MM et al. ASEPS-0 testbed interferometer. In: Breckinridge JB, editor. *Amplitude and Intensity Spatial Interferometry II.* Vol. 2220. SPIE; 1994. p. 89. DOI: 10.1117/12.177230

[32] Carleton NP et al. Current status of the IOTA interferometer. In: Breckinridge JB, editor. *Amplitude and Intensity Spatial Interferometry II.* Vol. 2200. SPIE; 1994. p. 152. DOI: 10.1117/12.177236

- [33] Baldwin JE et al. The first images from an optical aperture synthesis array: Mapping of Capella with COAST at two epochs. *A&A.* 1996;**306**:L13
- [34] Benson JA et al. Multichannel optical aperture synthesis imaging of zeta1 URSAE majoris with the navy prototype optical interferometer. *Astr. J.* 1997;**114**:1221-1226. DOI: 10.1086/118554
- [35] White NM et al. Progress report on the construction of the navy prototype optical interferometer at the Lowell Observatory. In: Breckinridge JB, editor. *Amplitude and Intensity Spatial Interferometry II.* Vol. 2200. SPIE; 1994. p. 242. DOI: 10.1117/12.177245
- [36] Le Bouquin JB et al. First observations with an H-band integrated optics beam combiner at the VLTI. *A&A.* 2004;**424**:719-726. DOI: 10.1051/0004-6361:20035849
- [37] McAlister HA et al. CHARA Array. In: Breckinridge JB, editor. *Amplitude and Intensity Spatial Interferometry II.* Vol. 2200. SPIE; 1994. p. 129
- [38] Berger JP et al. Integrated optics components for interferometric beam combination. In: *Astronomical Interferometry* Reasenberg RD, editor. *Proceedings of the Astronomical Telescopes and Instrumentation Conference, 20–28 March 1998.* Kona, HI, United States. Vol. 3350. SPIE; 1998. p. 898. DOI: 10.1117/12.317158
- [39] Malbet F et al. Integrated optics for interferometry. I. Concept and applications *Astron. Astrophys. Suppl. Ser.* 1999;**138**:1-10. DOI: 10.1051/aas:1999496
- [40] Berger JP et al. Integrated optics for astronomical interferometry II. First laboratory white-light interferograms. *Astron. Astrophys. Suppl. Ser.* 1999;**139**:173-177. DOI: 10.1051/aas:1999504
- [41] Haguenaer P et al. Integrated optics for astronomical interferometry III. Optical validation of a planar optics two-telescope beam combiner. *Applied Optics.* 2000;**39**(13):2130-2139. DOI: 10.1364/AO.39.002130
- [42] Berger JP et al. Integrated optics for astronomical interferometry IV. First measurements of stars. *A&A.* 2001;**376**:L31-L34. DOI: 10.1051/0004-6361:20011035
- [43] Laurent E et al. Integrated optics for astronomical interferometry V. Extension to the K band. *A&A.* 2002;**390**:1171-1176. DOI: 10.1051/0004-6361:20020404
- [44] Le Bouquin JB et al. Integrated optics for astronomical interferometry VI. Coupling the light of the VLTI in K band. *A&A.* 2006;**450**(3):1259-1264. DOI: 10.1051/0004-6361:20054258
- [45] Le Bouquin JB et al. First observations with an H-band integrated optics beam combiner at the VLT. *A&A.* 2004;**424**:719-726. DOI: 10.1051/0004-6361:20035849
- [46] Kanaan S et al. Disk and wind evolution of Achernar: The breaking of the fellowship. *A&A.* 2008;**486**:785-798. DOI: 10.1051/0004-6361:2007886
- [47] Bentini GG et al. Integrated Mach-Zehnder microinterferometer on LiNbO₃. *Optics and Laser Eng.* 2007;**45**:368-372. DOI: 10.1016/j.optlaseng.2005.05.006
- [48] Bentini GG et al. A new miniaturized optical system for chemical species spectroscopic detection based on a scanning integrated Mach-Zehnder microinterferometer on LiNbO₃. *Orig. of Life and Ev. of Biosph* 2006;**36**:597-603. DOI: 10.1007/s11084-006-9052-3